Received: 23 August 2023 | Revised: 31 January 2024 | Accepted: 18 April 2024

DOI: 10.1111/gbi.12600

gebiology WILEY

ORIGINAL ARTICLE

Energy flux couples sulfur isotope fractionation to proteomic and metabolite profiles in *Desulfovibrio vulgaris*

William D. Leavitt[1,2] | Jacob Waldbauer[3] | Sofia S. Venceslau[4] | Min Sub Sim[5] | Lichun Zhang[3] | Flavia Jaquelina Boidi[2,6] | Sydney Plummer[7] | Julia M. Diaz[7] | Inês A. C. Pereira[4] | Alexander S. Bradley[2,8]

[1]Department of Earth Sciences, Dartmouth College, Hanover, New Hampshire, USA

[2]Department of Earth and Planetary Sciences, Washington University in St. Louis, St. Louis, Missouri, USA

[3]Department of the Geophysical Sciences, University of Chicago, Chicago, Illinois, USA

[4]Instituto de Tecnologia Química e Biológica António Xavier, Universidade Nova de Lisboa, Oeiras, Portugal

[5]School of Earth and Environmental Sciences, Seoul National University, Seoul, South Korea

[6]Centro de Investigaciones en Ciencias de la Tierra (CICTERRA), CONICET-Universidad Nacional de Córdoba, Córdoba, Argentina

[7]Scripps Institution of Oceanography, University of California, San Diego, La Jolla, California, USA

[8]Division of Biology and Biomedical Sciences, Washington University in St. Louis, Saint Louis, Missouri, USA

Correspondence
William D. Leavitt, Department of Earth Sciences, Dartmouth College, Hanover, NH, USA.
Email: william.d.leavitt@dartmouth.edu

Present address
Sofia S. Venceslau, GenIbet Biopharmaceuticals, Oeiras, Portugal
Flavia Jaquelina Boidi, Instituto Nacional de Tecnología Agropecuaria (INTA), EEA, Rafaela, Argentina; and
Flavia Jaquelina Boidi, Instituto de Investigación de la Cadena Láctea (IDICAL), CONICET-INTA, Rafaela, Argentina

Funding information
National Science Foundation Graduate Reseearch Fellowship; National Science Foundation Division of Earth Sciences; Fundación Williams; FCT: Fundação para a Ciência e a Tecnologia; National Aeronautics and Space Administration; Argentina-Fulbright Program

Abstract

Microbial sulfate reduction is central to the global carbon cycle and the redox evolution of Earth's surface. Tracking the activity of sulfate reducing microorganisms over space and time relies on a nuanced understanding of stable sulfur isotope fractionation in the context of the biochemical machinery of the metabolism. Here, we link the magnitude of stable sulfur isotopic fractionation to proteomic and metabolite profiles under different cellular energetic regimes. When energy availability is limited, cell-specific sulfate respiration rates and net sulfur isotope fractionation inversely covary. Beyond net S isotope fractionation values, we also quantified shifts in protein expression, abundances and isotopic composition of intracellular S metabolites, and lipid structures and lipid/water H isotope fractionation values. These coupled approaches reveal which protein abundances shift directly as a function of energy flux, those that vary minimally, and those that may vary independent of energy flux and likely do not contribute to shifts in S-isotope fractionation. By coupling the bulk S-isotope observations with quantitative proteomics, we provide novel constraints for metabolic isotope models. Together, these results lay the foundation for more predictive metabolic fractionation models, alongside interpretations of environmental sulfur and sulfate reducer lipid-H isotope data.

KEYWORDS
chemostat, compound-specific hydrogen isotopes, microbial sulfate reduction, quantitative proteomics, stable sulfur isotopes

1 | INTRODUCTION

Sulfate-reducing microorganisms (SRMs) play a central role in Earth's carbon and sulfur cycles. Sulfate respiration by microorganisms has played a role in the Earth's carbon cycle for billions of years ever since sulfate became an abundant oxidant circulated by oceans and rivers (Fike et al., 2015; Lloyd et al., 2020). Extant SRMs degrade up to half the organic carbon in seafloor sediments (Bowles et al., 2014; Jørgensen, 1982; Jørgensen et al., 2019) and are integral in balancing Earth's oxidant budget through the production of iron sulfides (Berner & Canfield, 1989; Hayes & Waldbauer, 2006). Most marine sediments where sulfate reducers are active persist under severe energy limitation (Bradley et al., 2020; Jaussi et al., 2023; Jørgensen & Marshall, 2016). Tracing the metabolic activity of SRMs across energy gradients in nature is challenging given their rare doubling and low biomass. The distribution of natural abundance sulfur and hydrogen isotopes in the inorganic (sulfate and sulfide) and organic (lipid) byproducts of SRMs provides a record of microbial metabolic activity long after the environment and community have vanished. Moreover, little is known about sulfate-reducing bacterial protein dynamics in the face of chronic energy limitation. To address these limitations, we quantified the S isotope, proteome, lipid abundance, and lipid H-isotope phenotypes of energy limited sulfate reducers cultivated steady-state.

The majority of microbial sulfate reduction (MSR) occurs in marine sediments where energy supply is limited by the input of organic carbon, driving microbes in the system toward a state of persistent starvation (Bradley et al., 2020; Goldhaber & Kaplan, 1975; Jørgensen et al., 2019; LaRowe et al., 2020; Lever et al., 2015). Most laboratory MSR experiments, by contrast, are performed in closed ("batch") systems under conditions of energy and nutrient excess such that most experiments for S isotope or proteomic analysis are biased toward energy and nutrient replete and closed-system conditions. We do not know yet what occurs within the metabolic network of SRMs under the range of energetic regimes in either the lab or nature (Sim et al., 2023). This hinders the interpretive value of stable isotopes and metaproteomes in ecosystems where SRMs are major players.

Energy availability is a key determinant of microbial activity and the vigor with which biogeochemical cycles operate. Empirically derived energy flux versus isotope fractionation relationships (Leavitt et al., 2013; Sim et al., 2011) establish the basis for a range of models that incorporate sulfate reducer biochemistry and in vitro observations to sulfate reducer fractionation models (Bradley et al., 2011, 2016; Wenk et al., 2017; Wing & Halevy, 2014), yet many of the core assumptions in such models remain untested. In this study, we quantified shifts in the proteome of a model sulfate reducer under different energy availability, where sulfur isotope fractionation covaried with energy flux and cell specific sulfate reduction rate (csSRR; Figure 1). Given the central role of empirical data in building and testing such models, we sought to track the biochemical (proteomic and electron carrier) responses to differences in energy flux. Under different electron-donor-limited steady-state growth rates, we ask:

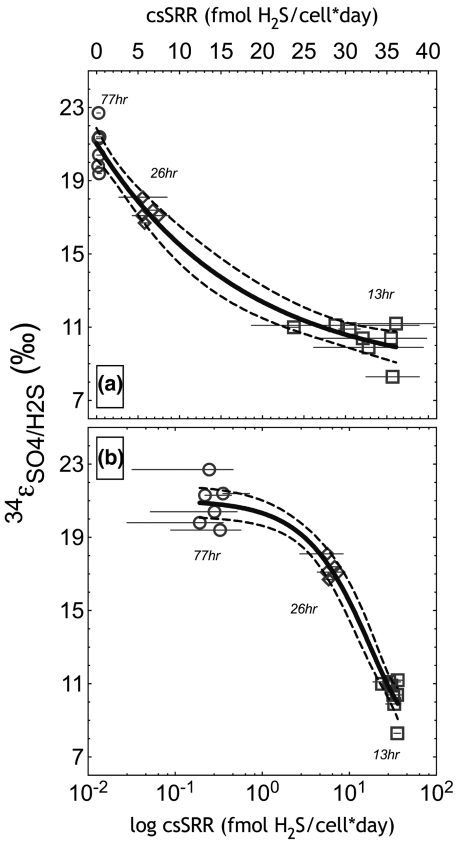

FIGURE 1 Sulfur isotope fractionation under three csSRR under electron-donor limitation. Either the (a) linear or (b) logarithmic *x*-axes of csSRR versus net isotope fractionation between residual sulfate in the effluent and accumulated product sulfide (*y*-axis). The nonlinear regression (Equation 3) was applied following Leavitt et al. (2013), to calculate the empirical fractionation limit ($^{34}\varepsilon_{sulfate/sulfide}$) ($r^2 = .97$) as a function of csSRR. The best-fit estimate (solid line) with 95% confidence intervals (dashed lines). The Y-intercept is 21 ± 0.8‰, Y-plateau is 8.3 ± 1.3‰, and the $k_\varepsilon = 0.056 \pm 0.015$. The 77 and 13 h endmember experiments are new to this study, while the 26-h data recalculated from Leavitt et al. (2019).

Do central metabolism protein abundances increase, decrease, or remain constant? Do intercellular reservoirs of sulfate reduction intermediates respond to change? Does the abundance or identity of electron carriers change at high versus low energy flux? In addressing these questions, we provide a set of new constraints for the next generation of isotope-metabolism models, which in turn will enable a more robust interpretation of sulfur isotopic records across environments and time periods.

2 | METHODS

The model sulfate-reducing bacterium *Desulfovibrio vulgaris* DSM644^T (WT) was cultivated following established protocols (Leavitt, Venceslau, et al., 2016), with the following modifications: chemostat media contained 30 mM lactate as the electron donor

and 30 mM sulfate as the electron acceptor, at 30.5 ± 0.1°C and pH 7.2 ± 0.1. We cultivated axenic populations of DSM644 at three distinct electron donor fluxes, where sulfate (terminal electron acceptor) and other nutrients (P, N, trace metals, vitamins) were provided in excess, whereas lactate (electron donor) influx limited growth and respiration. The three electron-donor fluxes (fast, medium, slow) capture three growth rates (see Section 3.1). Samples were taken after bioreactors completed at least five turnovers and had achieved steady state. The bioreactor (chemostat) systems are identical to those utilized recently for other DvH experiments (Leavitt et al., 2019). The slowest (77-h turnover time) and fastest (13-h turnover time) experiments were performed in duplicate parallel reactors for each rate, with a number of intervals sampled for bulk S isotopes, while for proteomics and cellular metabolites, samples are drawn only at one interval for each reactor (in technical replicate). For the intermediate rate (26-h turnover time), the experiments were performed in a single reactor, sampled at different turnover internals for both isotopes and proteomics, as previously reported (Leavitt et al., 2019). The sampling regime, analytical measurements, and calculations followed those in other recent sulfate reducer chemostat studies (Bradley et al., 2016; Leavitt et al., 2013, 2019), summarized below.

2.1 | Chemostat calculations

Dilution rate (D) of the chemostat reactor volume is calculated as

$$D = \frac{\text{liquid flux}}{\text{reactor liquid volume}} = \frac{\frac{\text{liters}}{\text{day}}}{\text{liter}} = \frac{1}{\text{day}} \quad (1)$$

The csSRR in an open system, where sulfate flux values may be substituted into Equation 2, when flux balance is conserved:

$$\text{csSRR} = \frac{\text{fmol sulfide produced}}{(\#\text{cells}/\text{volume}) \times (\text{reactor volume}) \times (\text{collection interval})} = \frac{\text{fmol sulfide}}{(\#\text{of cells}) \times \text{day}} \quad (2)$$

2.2 | Major reactant and product analyses

Extracellular sulfate and lactate samples were stored at −20°C until analysis. Lactate concentrations in fresh and spent media were determined by an Agilent 1100 HPLC (Agilent Technologies, Santa Clara, CA, USA) on an Aminex 87H column (Bio-Rad, Hercules, CA, USA). The sample was eluted with 8 mM sulfuric acid as an isocratic mobile phase at a flow rate of 0.6 mL/min, and the column effluent was passed through UV–visible and refractive index detectors. Sulfate concentrations in fresh and spent media were determined on a Dionex DX 500 ion chromatograph (IC) equipped with an AS11-HC column (Dionex, Sunnyvale, CA, USA), using a gradient elution with KOH as mobile phase. After electrochemical suppression, quantification was achieved with a conductivity detector.

For sulfide quantifications, the zinc acetate preserved samples (see trapping procedure in Leavitt et al., 2013) from each sample was quantified using a modified Cline method, as done previously (Cline, 1969; Leavitt et al., 2013). Analytical grade sodium sulfide (>98.9% $Na_2S{\cdot}9H_2O$) was used as the standard, and prepared in deoxygenated (boiled and N_2-sparged) growth medium, by precipitating the sodium sulfide with excess zinc acetate (anhydrous), mimicking the detailed protocol already published (Leavitt et al., 2014), with chemostat zinc-trap procedures following other recent chemostat studies (Leavitt et al., 2019).

2.3 | Bulk sulfur isotope analyses and S isotope notation

Bulk sulfur isotope analyses were performed on the medium sulfate, reactor sulfate, and trapped sulfide following a recent study (Leavitt et al., 2019). Samples for bulk S isotopes were the medium sulfate before it was allowed to enter the reactors, the residual dissolved sulfate removed from the reactors and after the reactors, and the microbialgenic sulfide removed from gas traps. The fractionation between sulfate and sulfide is calculated as $^{34}\varepsilon$ from the measured $\delta^{34}S$ values measured on trapped sulfate and sulfide. The variability in $^{34}S/^{32}S$ of a distinct S-bearing species or operationally defined pool, y, is reported as $\delta^{34}S_y$ (Equation 3a). The difference between two pools, such as sulfate (A) and sulfide (B), is Equation 3b (y = A or B) and is reported in alpha (Equation 4a) or epsilon (Equation 4b) notation, where the latter is in permille.

$$\delta^{34}S_y = \left[\left(^{34}S/^{32}S\right)_{\text{sample}}\right] / \left[\left(^{34}S/^{32}S\right)_{\text{standard}} - 1\right] \times 1000 \quad (3a)$$

$$\delta^{34}S_{A-B} = \left(^{34}\alpha_{A-B} - 1\right) \times 1000 \quad (3b)$$

$$^{34}\alpha A - B = \left[\left(^{34}S/^{32}S\right)_A / \left(^{3x}S/^{32}S\right)_B\right] \quad (4a)$$

$$^{34}\varepsilon A - B = \left(^{34}\alpha - 1\right) \times 1000 \quad (4b)$$

2.4 | Rate–fractionation model

We applied the nonlinear regression one-phase decay model to the net S-isotope fractionation and specific rate estimates developed in a prior study (Leavitt et al., 2013). Results of the model fit and standard error estimates, fitting parameters and their standard errors, and the 95% confidence intervals (dashed lines) are presented in Figure 1. The fitted rate constant is first order with respect to the rate-limiting reactant (electron donor, lactate). This assumption is valid because the growth and respiration of *D. vulgaris* chemostat

populations are limited by electron donor influx, whereas terminal electron acceptor sulfate is always present in excess. The nonlinear rate/fractionation model is presented in Equations 5 and 6.

$$\mathrm{csSRR} = \frac{\ln\left(\frac{{}^{34}\varepsilon_{\mathrm{MSRobs}} - {}^{34}\varepsilon_{\mathrm{MSRmin}}}{{}^{34}\varepsilon_{\mathrm{MSRmax}} - {}^{34}\varepsilon_{\mathrm{MSRmin}}}\right)}{-k_{\varepsilon_{\mathrm{MSR}}}} \quad (5)$$

$$\mathrm{csSRR}^{-1} = \frac{k'_{\varepsilon_{\mathrm{MSR}}}}{\left({}^{34}\varepsilon_{\mathrm{MSRmax}} / {}^{34}\varepsilon_{\mathrm{MSRobs}}\right) - 1} \quad (6)$$

Data inputs are the measured (observed) ${}^{34}\varepsilon_{\mathrm{MSRobs}}$ for a given dilution rate (D) and the corresponding csSRR. Fitting parameters are as follows: k, a pseudo-first order rate constant specific to each non-linear regression (k_{ε}, k'_{ε},); ${}^{34}\varepsilon_{\mathrm{MSRmax}}$, the theoretical maximum fractionation as csSRR^{-1} approaches infinity (which physically corresponds to D approaching zero); and in the case of the one-phase decay model (Equations 3 and 4) the ${}^{34}\varepsilon_{MSRmin}$ corresponds to the classically defined "plateau," where the minimum value corresponds to the rate-limiting step in sulfate reduction when *D. vulgaris* grows and metabolizes at its μ_{max}.

2.5 | Intracellular S-metabolite abundance and S-isotope analyses

Intracellular sulfur metabolite quantification and S-isotope analysis were performed using preparative ion chromatography coupled to multicollector inductively coupled plasma mass spectrometer (MC-ICP-MS) at the California Institute of Technology. The experimental and analytical procedures are described in greater detail elsewhere (Sim et al., 2017) and summarized here. Biomass samples from the 13-and 77-h reactors were washed with anaerobic cold saline solution to remove culture medium constituents and flash frozen in liquid nitrogen until extraction. The frozen pellet was thawed and resuspended in 0.6-mL degassed deionized water (DW) under an anaerobic atmosphere of nitrogen: hydrogen (90:10) (Coy Manufacturing Co., Ann Arbor, MI, USA). After mixing with an equal volume of cold methanol, the sample was left on dry ice for 30 min and then thawed on ice for 10 min in 20 μL of 50 mM zinc chloride and 100 μL of 13 mM formaldehyde were added to prevent the oxidation of sulfide and sulfite, respectively. The supernatant was recovered by centrifugation. Sulfur metabolites, sulfate, sulfite, and APS, were quantified by IC using a gradient dilution with KOH as mobile phase, and the eluent fractions corresponding to sulfate and APS were collected for isotopic analysis. Collected APS was quantitatively converted to sulfate via hydrolysis under acidic conditions. Then samples containing dissolved sulfate were dried on a hot plate and diluted in 5% nitric acid to a sulfate concentration of 20 μM to match the in-house working standard. S isotope analysis was carried out following the original method (Paris et al., 2013) via MC-ICP-MS (Thermo-Fisher Scientific Neptune Plus, Bremen, Germany). Sulfur isotope ratios of the sample and working standard were measured alternately, and instrumental blank was estimated after each block. The mean blank value was subtracted from the measured signal for ^{32}S and ^{34}S, and the measured $^{34}S/^{32}S$ ratios were calibrated using a linear interpolation between the two bracketing standard values.

2.6 | Cell-associated (in)soluble redox intermediates

Menaquinone and NAD(P)(H) levels in 13- and 77-h biomass samples were measured at the Proteomics & Mass Spectrometry Facility at the Danforth Plant Science Center, following established methods (Arrivault et al., 2009; Lunn et al., 2006). Biomass pellets were prepared as noted above for intracellular S metabolite analyses by cold centrifugation and flash-freezing. The nicotinamide cofactors were quantified using a custom LC–MS, an Eksigent MicroLC and Thermo Q-Exactive using a 0.5 × 50-mm Sepax Proteomix SAX column. Samples were extracted using a protocol modified from (Lunn et al., 2006). The samples were dissolved in 100 μL of water, and then 1 μL was injected onto the LC–MS. The solvents were 25% methanol (B) and 250 mM $(NH4)_2CO_3$. The gradient started at 100% B after a hold for 3 min. The composition was adjusted to 50% over 5 min, followed by a ramp to 0% B over 3 min with a hold for 1 min, then back to 100% B over 2 min, followed by a re-equilibration for 12 min. The flow rate was 15 μL per minute. Data were recorded in negative profile mode from m/z 200–1000 with a resolution setting of 70,000 (at m/z 200). Peak areas were extracted and normalized against the area for MOPS (internal standard).

A total of six samples were analyzed for the presence of menaquinones MK-5 and MK-6 using MK-4 as a standard. These compounds were analyzed from the organic fraction of the extraction above using a custom Eksigent MicroLC and Thermo Q-Exactive using a 0.5 × 100-mm custom-packed PLRPS column. The solvents were water with 0.1% formic acid (A) and acetonitrile with 0.1% formic acid (B). The gradient started at 30% B after a hold for 3 min. The composition was adjusted to 100% B over 3 min with a hold at 100% B for 2 min, followed by a ramp back to 300% B over 2 min, followed by a re-equilibration for 6 min. The flow rate was 15 μL/min. Data were recorded in positive profile mode from m/z 400 to 700 with a resolution setting of 140,000 (at m/z 200). These quantities are measured relative to the internal analytical standard (MK-4), and then normalized for cell numbers such that sample size or cell number is not the explanatory variable.

2.7 | Cell counting

Cell counts were conducted on a Guava EasyCyte HT flow cytometer (Millipore). Flow cytometry samples were preserved in 0.5%

glutaraldehyde (final concentration) and stored at −80°C prior to analysis. For analysis, samples were diluted (1:100) with filtered seawater (0.01 μm), stained with SYBR Green I (Invitrogen) according to the manufacturer's instructions, and incubated in a 96-well plate in the dark at room temperature for 1 h. Samples were analyzed at a low flow rate (0.24 μL/s) for 3 min. Cells were gated and counted based on diagnostic forward scatter versus green fluorescence signals. Instrument-specific beads were used to validate performance of the cytometer prior to sample analysis.

2.8 | Proteomics

Samples for proteomics were collected and analyzed as in Leavitt et al. (2019), with quantitation by diDO-IPTL in vitro peptide isotope labeling (Waldbauer et al., 2017). The false discovery rate (FDR) for peptide-spectrum matches was controlled by target-decoy searching to <0.5%, using the translated genome of *Desulfovibrio vulgaris* DSM 644^T obtained from MicrobesOnline (http://www.microbesonline.org/) and Integrated Microbial Genomes (IMG; http://img.jgi.doe.gov/) as a search database. Protein-level relative abundances and standard errors were calculated in R using the Arm postprocessing scripts for diDO-IPTL data (Waldbauer et al., 2017; github.com/waldbauerlab).

Significantly differential protein expression between experimental conditions was determined using a *Z*-score for protein abundance differences by taking the difference in the mean ($\log_2$-transformed) protein abundance between conditions and dividing it by the sum of the total uncertainty estimate for that protein in the two conditions. This total uncertainty estimate for a given condition was taken as the root-square sum of the standard deviation of a protein's abundance across the biological replicates of that condition plus the average standard error of the protein's abundance across quantified spectra within each replicate. These *Z*-scores were converted to *p*-values assuming a standard normal distribution and then the familywise error rate for significantly differential expression between conditions was controlled using the *q*-value method to correct for multiple testing (Benjamini & Hochberg, 1995).

2.9 | Fatty acid abundances and lipid hydrogen isotope compositions

Cells from each of the 13- and 77-h reactors were pelleted and freeze-dried after sampling by cold centrifugation. Fatty acid extraction, derivatization to fatty acid methyl esters (FAMEs), and analyses were performed following other studies on SRMs (Leavitt, Flynn, et al., 2016; Leavitt, Venceslau, et al., 2016). The FAME retention times and peak areas were determined by gas chromatography (GC) with thermal conductivity detection (TCD), and the δ^2H values of lipids were measured by GC high temperature conversion isotope ratio mass spectrometry (GC-HTC-IRMS) following recent studies (Leavitt, Flynn, et al., 2016; Leavitt, Venceslau, et al., 2016). Each fatty acid from each sample was measured for δ^2H at a minimum of 3×, for a total of 3-technical replicates on each of the 2× biological replicates per sampling interval per reactor per rate. Hydrogen isotope compositions of medium waters were measured following established methods (McFarlin et al., 2019; Taenzer et al., 2020). The variability in ^{2}H/^{1}H of a measured pool, *y*, is reported as δ^2H_y (Equation 7) relative to V-SMOW (Vienna Standard Mean Ocean Water). Similar to differences in S-isotope pools, the H-isotope fractionation is reported between medium water and a specific lipid, or the weighted abundance of all lipids in a given can be reported in alpha (Equation 8b) or epsilon (Equation 8b) notation.

$$\delta^2H_y = \left[\left(^2H/^1H\right)_{sample}\right] / \left[\left(^2H/^1H\right)_{standard} - 1\right] \times 1000 \quad (7)$$

$$^2\alpha\text{lipid / water} = \left[\left(^2H/^1H\right)_{lipid} / \left(^2H/^1H\right)_{water}\right] \quad (8a)$$

$$^2\varepsilon\text{lipid / water} = \left(^2\alpha\text{lipid / water} - 1\right) \times 1000 \quad (8b)$$

3 | RESULTS

In this study, we cultivated model sulfate reducer *Desulfovibrio vulgaris* DSM644^T under three different steady-state conditions each limited by electron donor (Figure S1). From all conditions (fast, medium, slow), we quantified net sulfate/sulfide S isotope fractionation and protein-level gene expression. While we also quantified the intracellular sulfate S isotope compositions, cellular S metabolite abundances, lipid/water H isotope fractionation, and electron carrier abundances from only the fast and slow conditions, each chemostat steady-state and related rates yielded statistically unique responses in each category.

3.1 | Sulfate reduction rates, S-isotope fractionation, and core S-metabolites

In each experiment, sulfate reduction rate scaled with bioreactor turnover time, and in turn, net sulfur isotope fractionation between reactant sulfate and product sulfide scaled with cell-specific sulfate reduction rates. The average reactor turnover times (τ) were 13 ± 1 h (fast), 26 ± 2 h (medium), and 77 ± 5 h (slow), which corresponded to estimated cell-specific sulfate reduction rates (csSRR) of 31.9 ± 5.6, 6.2 ± 1.4, and 0.3 ± 0.2 fmol per cell per day (Figure 1). The average sulfur isotope fractionation values between reactant sulfate and product sulfide, $^{34}\varepsilon_{SO4/H2S}$, were 21 ± 1‰, 17 ± 1‰, and 10 ± 1‰, from slowest to fastest, respectively (Figure 1), and are significantly different between the three rates. A nonlinear one-phase decay model is fit to the rate versus fractionation relationship, following a prior use case (Leavitt et al., 2013).

The abundance of key sulfate reduction intermediates scales with electron donor flux. The relative abundance of intracellular metabolic intermediates from the fast ($\tau = 13$ h) and slow ($\tau = 77$ h) populations tracked the net rate, specifically the relative quantities of biomass-associated (intracellular) sulfate, APS, and sulfite. The intracellular sulfate, APS, and sulfite levels were consistently higher in the fastest (13 h) relative to slowest (77 h) doubling populations, respectively (Figure 2a). Intracellular sulfate-S isotope compositions were measured at the fastest and slowest turnover times (Figure 2b). Intracellular sulfate S-isotope values are enriched by 6.5 and 7.7‰, relative to the residual sulfate in the reactors, from the fast turnover times ($\tau = 13$ h) reactors. In the slowest turnover time experiments ($\tau = 77$ h), intracellular sulfate S isotope values were only 1.1 and 1.2‰ enriched relative to residual reactor sulfate (Figure 2b). The directionality of this enrichment is consistent with a recent suite of batch experiments (Sim et al., 2017). Rate and model calculations are detailed in the Section 2.

3.2 | Lipid abundance, lipid H-isotope values, lipid and soluble electron carriers

To determine if growth rate—limited by electron donor flux—is recorded in either membrane lipid profiles or lipid H-isotope values, we measured the relative abundance of different fatty acids (FA), the hydrogen isotope composition of those FAs, and the menaquinone and NAD(P)(H) abundances from the 13- and 77-h rate regimes.

Each *D. vulgaris* population produced abundant FAs with differing quantities of *iso*-, *anteiso*-, and *n*- fatty acids between 15 and 19 tail carbons, with 0 to 1 double bonds, and small quantities of 3-hydroxy-$C_{18:0}$. The faster growing *D. vulgaris* produced FA profiles composed of about 35% *iso*-$C_{17:1}$, with each other FA making up no more than 10% each, whereas the 77-h membranes were composed of ~25% *iso*-$C_{17:1}$, with ~17% *n*-$C_{18:1}$ (Figure 3). The largest differences in FA abundances between the 13- and 77-h *D. vulgaris* populations were shifts in *iso*-$C_{17:1}$ and in *n*-$C_{18:1}$ (Figure 3). Meanwhile, the hydrogen isotopic composition of the different fatty acids captured a consistent pattern between the fastest versus the slowest populations. Overall, a small but reproducible shift was apparent, with more depleted values in the faster 13-h cells relative to the slow 77-h cells. The mass-weighted average fractionation between lipids and growth water ($^2\varepsilon_{l/w-total}$) for the 77-h cells is −158‰, as opposed to −175‰ for the 13-h cells ($2\sigma = 8$‰). The compound-specific fractionation values ($^2\varepsilon_{lipid/water}$) for each individual lipid were also greater in the slowest relative to fastest growing cells (Figure 3b). The most depleted lipid for each rate condition was *anteiso*-$C_{17:1}$, where the most enriched were *n*-$C_{17:1}$ and *n*-$C_{18:1}$. The isotopic ordering of individual lipids ($^2\varepsilon_{lipid/water}$) was similar for both populations (Figure 3b).

The relative quantities of membrane-associated electron carriers menaquinone 5 and 6 (MK-5, -6) and soluble electron transfer intermediates NADP(H) and NAD(H) were measured on biomass from the $\tau = 13$- and 77-h reactors. More NADH was found in $\tau = 13$ h relative to 77-h cells, and NADPH was only detectable in 13-h cells (Figure S2A). Similarly, more of both MK's were present in the 13 h cells (Figure S2B), and while NAD(P)(H) levels were more variable between replicates, likely due to our sampling strategy, the general trend showed more of all oxidized H-shuttles, NAD^+ and $NADP^+$, in the 13-h cells, which were both orders of magnitude more abundant than their reduced counterparts in both populations. Future applications of these measurements require a more robust method to generate high fidelity estimates (García et al., 2018).

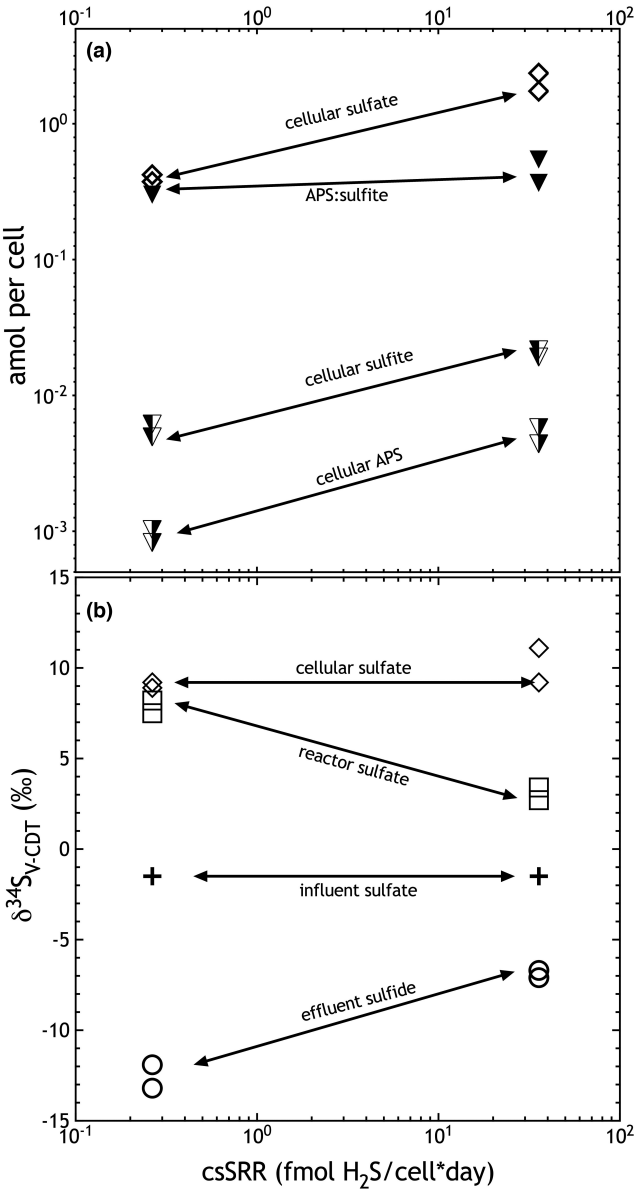

FIGURE 2 Sulfur isotopes and S metabolites from the slowest (77 h) and fastest (13 h) reactors. (a) attomole per cell quantities of intracellular sulfate, APS, and sulfite, as well as the APS:sulfite per cell ratio. (b) Sulfur isotope compositions of reactant (influent) sulfate, intracellular sulfate, residual reactant (reactor) sulfate, pooled product effluent) sulfide; and the offset between reactor sulfate and effluent sulfide in (b) gives the estimates of $^{34}\varepsilon_{sulfate/sulfide}$ in Figure 1.

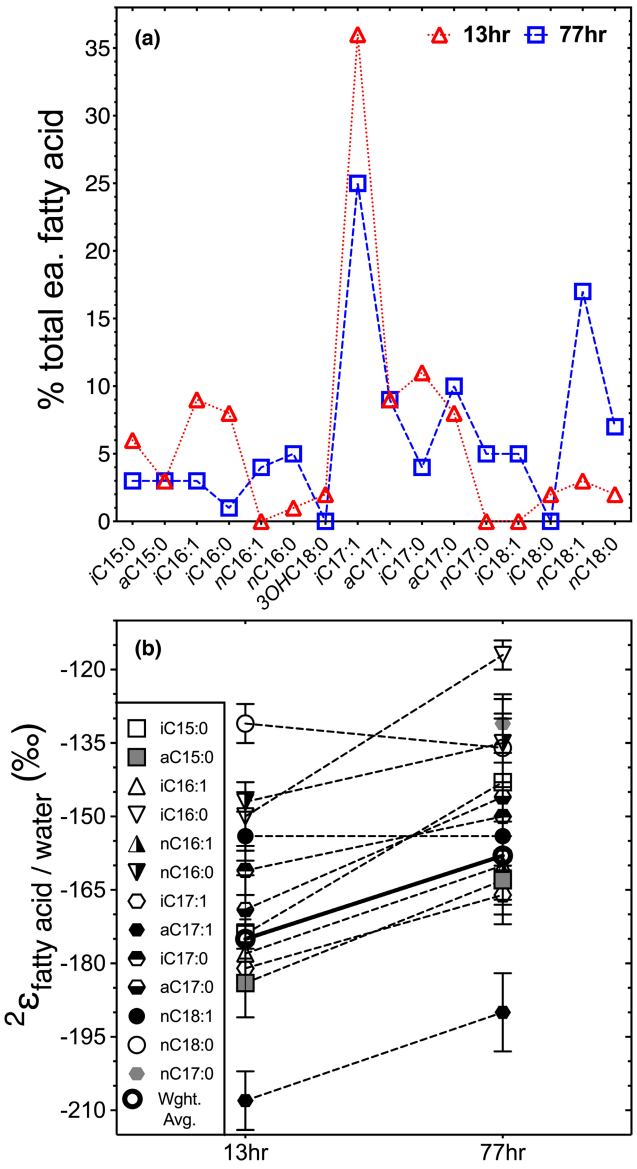

FIGURE 3 The *Dv*H lipid abundance and lipid/water H-isotopes. (a) Fatty abundances from the 13 h (red dotted line and triangles) and 77 h (blue dashed line and squares). (b) The $^2\varepsilon_{lipid/water}$ values for individual fatty acids, as well as the abundance the weighted average (heavy open circle) for the 13-h vs. 77-h chemostat grown cells.

3.3 | Proteomic response to changes in energy flux

To identify how protein expression modulates energy metabolism at each electron-donor flux, we quantified the whole proteome response in the *D. vulgaris* population at each steady-state growth rate. We quantified 387 proteins at all rates, in all replicate reactors, across all sampling intervals (Figure S3), representing 11% (387 of 3535) of all predicted protein-coding genes in *Desulfovibrio vulgaris* DSM 644^T. To understand how protein expression patterns and COGs correlate to the magnitude of sulfur isotope fractionation, we focus on proteins where abundance increased or decreased significantly *with* or *inverse* to csSRR ($q < 0.05$). Of the aforementioned 387 proteins, 37 increased in abundance as csSRR increased (more in 13 h > 26 h > 7 h), versus 28 that increased in abundance inverse to csSRR (most abundant in 77 h > 26 h > 13 h). Of the 37 up with rate, 11 are from "energy production and conversion" COG category, 12 from translation and ribosome production, 7 of unknown function, and the other 7 across four other COG categories (see Table 1). The large number of ribosomal proteins in fast (13 h) populations is consistent with prior observations, where the relationship between bacterial cell growth, translation rates, and ribosome abundance covaries (Bosdriesz et al., 2015; Klumpp et al., 2013). From the 28 scaled inverses to rate, only 2 were from translation and ribosome biogenesis, whereas 9 are from energy production and conversion and four from unknown functions, with the remaining 13 scattered across other COG identifiers (Table 1). From those same 65 proteins, a clear secondary COG function was also identified for 5 of them (Table 1). Below, we focus primarily on the energy and carbon metabolism proteins (COG category C) that are most likely involved in catabolic S and anabolic H isotope fractionation. These proteins are summarized in Figure 4 (and Figure S4) and discussed below.

4 | DISCUSSION

In this study, we show how environmental conditions influence inorganic ($^{34}\varepsilon_{SO4/H2S}$) and organic ($^2\varepsilon_{lipid/water}$) biosignatures with the model sulfate reducer, *D. vulgaris*. Experimentally imposed shifts in cell-specific growth and metabolic rates (csSRR) due to different electron donor flux yield clear shifts in key protein and metabolite abundances, lipid abundance and H-isotope values, cellular S-metabolites, and net S isotope values. While the experiments herein cover a smaller range of csSRR and concomitant $^{34}\varepsilon_{SO4/H2S}$ than prior chemostat studies (Chambers et al., 1975; Leavitt et al., 2013; Sim et al., 2011), the novel suite of tools we employ to quantitatively track physiological (proteomic, metabolite), organic (lipid/water), and inorganic (sulfate/sulfide) isotope responses provide a new window into how sulfate reducing bacteria operate at different energy availabilities.

4.1 | Energy flux drives shifts in key proteins and metabolites

The abundance of some energy metabolism proteins is clearly coupled to shifts in csSRR and $^{34}\varepsilon_{SO4/H2S}$ (Figure S4). Some, but not all, core sulfate respiration and energy metabolism proteins scaled positively or negatively with energy flux (Figure 4). The *proteins that decreased* as *energy flux decreased* (Figure 4b) include those integral to APS reduction to HSO_3^-/SO_3^{2-} (ApsAB, QmoAB, PpaC)—together these proteins are part of the Rex regulon, which is a repressor of sulfate adenylyl transferase that is regulated by NADH (Christensen et al., 2015). Given that APS reduction is the

TABLE 1 The differentially expressed proteins in *Dv*H with rate, by COG. The number of proteins by COG category increased or decreased consistently with electron donor regulated rate. (+) positive abundance scaling with csSRR versus (−) inverse abundance with csSRR.

		COG primary function			COG secondary function		
COG	Function	# proteins	(+) rate	(−) rate	# proteins	(+) rate	(−) rate
B	Chromatin structure and dynamics	1	0	1	0	0	0
C	Energy production and conversion	20	11	9	0	0	0
E	Amino acid transport and metabolism	4	1	3	0	0	0
H	Coenzyme transport and metabolism	0	0	0	1	1	0
I	Lipid transport and metabolism	3	2	1	0	0	0
J	Translation, ribosomal structure, biogenesis	14	12	2	0	0	0
N	Cell motility	2	0	2	0	0	0
O	Post translational modification, protein turnover, chaperones	4	3	1	0	0	0
P	Inorganic ion transport and metabolism	1	0	1	0	0	0
Q	2′ metabolites biosynthesis, transport, catabolism	0	0	0	1	0	1
R	General function prediction only	0	0	0	0	0	0
T	Signal transduction mechanisms	5	1	4	3	0	3
X	Unknown function	11	7	4	0	0	0
	Sub-totals	65	37	28	5	1	4

first step in MSR to link sulfate respiration to membrane-bound electron transport (and hence energy conservation) via the Qmo complex, this reveals the cellular scale coupling of MSR proteins to environmental limitation in electron donor, and the consequences for intracellular S intermediates and isotopes (Figure 2). On the anabolism side, part of the NADPH/NADH electron-bifurcating transhydrogenase (NfnB) was much less abundant at low csSRR (Figure 4b). Nfn likely plays a significant role in sulfate reducer lipid-H isotope fractionation (Leavitt, Flynn, et al., 2016), and so the decrease in this system may have played some role in the shifts in the lipid-H compositions we observed (Figure 3). The direction of catabolic S isotope fractionation, lipid-H isotope fractionation, protein, and NADH observations is coherent when viewed through the lens of the Rex regulon response to NADH availability at high electron donor flux.

Under electron-donor limitation energy proteins that *significantly increased* in abundance include subunits of both membrane and soluble proteins (Figure 4a). These include the membrane Ech hydrogenase and Rnf complex and an alcohol dehydrogenase (Ald). The Hdr/Flx complex interacts with the ferredoxin reservoir, as well as NAD(H) and alcohol dehydrogenase, which may indicate that ferredoxin becomes less reduced under low electron donor availability (Ramos et al., 2015), enabling lower flux of reductant to the sulfate reduction machinery, enabling a larger S-isotope fractionation (Figure 1) while simultaneously influencing lipid H-isotope fractionation via the Nfn and NAD(P)(H) reservoirs (Figures 3 and 4; Figure S3).

4.2 | Changes to $^{34}\varepsilon_{SO4/H2S}$ and $^{2}\varepsilon_{lipid/water}$ reflect shifts in catabolism and anabolism, respectively

The cascade of catabolic and anabolic processes *Dv*H operates modulated S and H isotope fractionation profiles, respectively. As predicted, $^{34}\varepsilon_{SO4/H2S}$ correlated inversely and non-linearly with cell specific sulfate reduction rate, and both responded directly to energy limitation. As csSRR rates slow in response to decreased electron donor flux, the intracellular abundances of key MSR intermediates sulfate, APS, and sulfite decrease, as does the isotopic offset between intra- and extracellular sulfate (Figure 2), even as the net fractionation between pooled product sulfide and residual reactant sulfate increases. In a recent study performed with batch cultures that ran at effectively high csSRR, intracellular sulfate was more than 50‰ enriched relative to the extracellular sulfate, even when the net fractionation between sulfate and sulfide was an order of magnitude less at 4‰ (Sim et al., 2017). Together, the prior batch data from Sim et al. (2017) and similar observations from these chemostats indicate that the predicted equilibrium isotope effect between sulfate and sulfide is approached intracellularly when sulfate is available in excess of electron donor. The near-equilibrium isotope effect is minimally expressed when csSRR are rapid due to cellular-scale isotope distillation; conversely, the net sulfate/sulfide fractionation values are nearer to equilibrium when csSRR rates and mass transfer are slow, and less influenced by localized (cellular) distillation. Put differently, the large fractionation predicted from equilibrium theory between sulfate

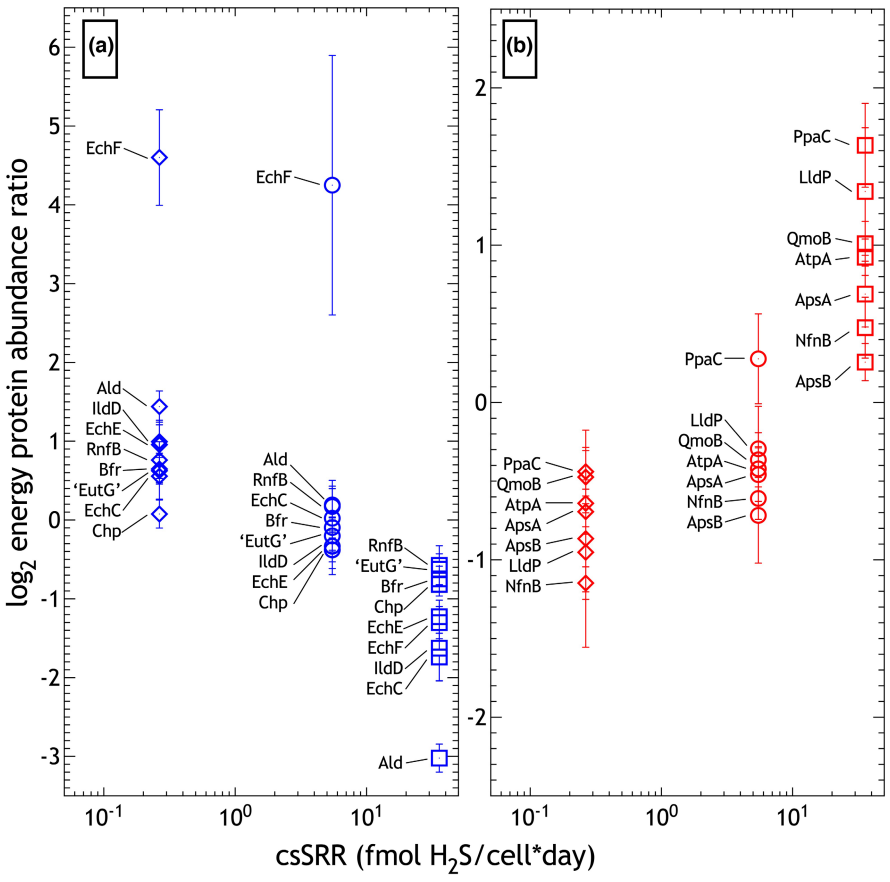

FIGURE 4 The core sulfate reduction and energy metabolism proteins in *Dv*H that vary with csSRR. (a) Energy proteins that most increased in abundance when reductant-limited growth and csSRR were decreased (inverse relationship between abundance and rate). (b) Energy proteins that most increased in abundance as growth and csSRR increased (positive relationship between abundance and rate). The *y*-axes are plotted on the same scale in Figure S4.

and sulfide is masked by rapid forward reaction rates at the cellular and even enzyme level (Leavitt et al., 2014; Sim et al., 2023; Thode et al., 1961). Large fractionations can only be expressed when net reaction rate slows, and the intracellular isotope effects are summed into the expressed net fractionation values, as has been proposed in some metabolic isotope models (Bradley et al., 2011; Brunner & Bernasconi, 2005; Farquhar et al., 2007; Johnston et al., 2007; Rees, 1973; Sim et al., 2019, 2023), but had not been seen until the work by Sim et al. (2017) and now here. Furthermore, because MSR likely operates as a branched metabolic network (Badzjong & Thauer, 1980; Bradley et al., 2011), the observed nonlinear relationship between csSRR and $^{34}\varepsilon_{SO4/H2S}$ (Leavitt et al., 2013; Sim et al., 2011) remains a challenge to reproduce in models without significant parameterization. Empirical calibrations across a range of organisms and environmental conditions are likely the best option in providing constraints on more nuanced metabolic isotope models.

Lipid-H isotope compositions and electron transfer intermediates also scaled in abundance with electron donor flux and csSRR. The $^{2}\varepsilon_{lipid/water}$ weighted average in the fastest *Dv*H (13 h) populations were −175‰ relative to the slowest (77 h) populations −158‰ (Figure 3b), with lipid-specific isotope pattern (i.e., chain length and iso−/anteiso−/*n*-) following prior observations for fatty acids from sulfate-reducing bacteria (Campbell et al., 2009, 2017; Dawson et al., 2015; Leavitt et al., 2017, 2019; Leavitt, Flynn, et al., 2016; Leavitt, Venceslau, et al., 2016; Osburn et al., 2016). In addition to fatty acids, more membrane-bound electron transfer intermediates menaquinone-5 and -6 are present in 13-h relative to 77-h cells (Figure S2B). Beyond *Dv*H, the trend of more depleted lipids at higher growth rates is consistent with batch experiments utilizing other sulfate reducers across a range of carbon and energy sources (Leavitt, Flynn, et al., 2016; Osburn et al., 2016). We also provide coarse estimates of the soluble NAD(P)(H) reservoirs, which were all higher in the faster cells (Figure S2A), where we also observed increased NfnB expression at higher energy flux (conversely less NfnB at lower energy flux, Figure 4b). This is broadly consistent with two studies in a sulfate reducer and fermenter, where genes (*nfnAB*) encoding the NADP(H)/NAD(H) electron-bifurcating transhydrogenase were genetically disrupted, which forced the organisms to grow more slowly than the respective wildtypes and led to less $^{2}\varepsilon_{lipid/water}$ fractionation (Leavitt et al., 2017; Leavitt, Flynn, et al., 2016). These results are consistent within anaerobic bacteria that utilize the Nfn transhydrogenase, where the broader observation of less lipid/water H-isotope fractionation at lower growth rates, perhaps due to lower energy flux (Leavitt et al., 2017; Leavitt, Flynn, et al., 2016; Osburn et al., 2016). These observations across experiment types indicate a central role for energy availability in setting the net $^{2}\varepsilon_{lipid/water}$ values, primarily via the recording of intracellular NADPH/NADH (im)balances in lipid-H isotope compositions (Wijker et al., 2019). Future works might track Domain or metabolism-specific lipids and lipid-H isotope values across environmental energy gradients,

particularly in systems where direct cultivation or activity assays are not practical or yet possible, for example, deep subsurface sediments, subglacial lakes, and deep fracture fluids (Bradley et al., 2020; Drake et al., 2018; Lever et al., 2015).

4.3 | Framework to interpret the response of sulfate reducers to energy limitation

A theme emerges that ties together *D. vulgaris*' response to different reductant availability as they are expressed in inorganic S and organic H isotopes, protein, and metabolites.

4.3.1 | High energy flux

When electron and carbon source flux is highest (13 h population), DvH cells must transfer reducing equivalents onto sulfate with maximum efficiency. To process incoming reducing equivalents, cells in the 13-h chemostats maintain high stocks of the MSR intermediates APS and sulfite (Figure 2b), while also accumulating a larger intracellular pool of the terminal electron acceptor sulfate (Figure 2b). This is also seen in the higher abundance of AprAB and QmoAB proteins in the 13-h cells (Figure 3b), and increased menaquinone levels in the faster growing cells (Figure S2B). This enables efficient electron transport to and through the membrane and the rapid reduction of sulfate, which then limits the expressed S isotope fractionation between sulfate and sulfide (Figures 1 and 2a). The larger standing pools of electron transfer (MK) and reducing equivalents in the faster 13-h cells is broadly consistent with a higher availability of electrons under the higher reductant flux regime. This indicates that the DvH populations that experienced larger electron donor fluxes were able to build transmission capacity, which again enabled faster sulfate respiration. This is consistent with the protein and S-metabolite data, where higher abundances of the QmoAB electron transfer proteins, more intracellular sulfate sulfite, and APS at the faster csSRR, all converge to generate smaller net S isotope fractionation values and larger net H isotope values.

4.3.2 | Low energy flux

During severe electron donor limitation, APS reductase and QmoAB were less expressed and likely csSRR decreased, which are reflected in the increased $^{34}\varepsilon_{\text{sulfate/sulfide}}$. The control energy flux exerts on csSRR and $^{34}\varepsilon_{\text{sulfate/sulfide}}$ appears to be mediated by APS reductase abundance. While it is possible csSRR could be under post-translational control, the near constant ratios of APS:sulfite in both the 13- and 77-h conditions suggest that increased flux through that step of sulfate reduction is indeed controlled by APS reductase abundance. Still, further testing of this hypothesis will require independent genetic control of AprAB abundance. Broadly, these findings agree with two recent batch-culture studies by Sim and colleagues (Sim et al., 2017, 2019). With energy least available in the 77-h chemostats, electron donor overburden was not as much of a challenge, intracellular sulfate concentrations and sulfate reduction metabolites were lower (Figure 2b), and the S-isotope offset between extra- and intracellular sulfate was eliminated. Enzymes needed to reduce sulfate to sulfite were in lower demand (cf. AprAB, QmoAB), whereas proteins that enable more efficient energy acquisition from the carbon and electron donor (Ldh, Por, Pta, Ack) were then in higher demand, as were those needed to couple electron transfer to membrane redox potential (cf. Ech, Tmc, Rnf) and to facilitate cytoplasmic electron transfer (Flx/Hdr, certain Adh's) (Figure 5). These observations are consistent with the notion that as biochemical reducing equivalents became less available due to lesser lactate influx, the DvH cells increased the abundance of the key, perhaps high affinity, Ech hydrogenase to maintain proton motive force in the face of lower energy flux. The large increase in the membrane energy metabolism Rnf complex (Figure 4a), which links the NADH and ferredoxin pools, is likely a reflection of the need for energy to continue through the system at lower flow rates. Consistent with this concept, we observe more membrane-bound and soluble electron transfer machinery at the lowest power regime (77 h; specifically, Ech, Rnf, Hdr/Flx, Por, Aor), as compared to more sulfate-activation machinery in the intermediate (26 h), and especially fastest (13 h) conditions—specifically, more ApsR and Qmo (Figures 4 and 5). Taken together, it is most likely that APS reductase expression and the Rex regulon most modulate variation in $^{34}\varepsilon_{\text{SO4/H2S}}$ and $^{2}\varepsilon_{\text{lipid/water}}$ across the different energy limited conditions in these experiments.

4.3.3 | Remaining challenges

While the approaches here shed much light on the relationship between thermodynamic drive and net catabolic isotope fractionations, it remains unclear if the major intracellular electron carriers change in response to energy flux. It was predicted that different electron carriers are utilized under different power regimes (Wenk et al., 2017; Wing & Halevy, 2014), which may include ferredoxin (−398 mV); two forms of flavodoxin (−371 and −115 mV); cytochrome c_3 (−290 mV); menaquinones (−74 mV) and rubredoxin (−57 mV) – midpoint potentials from Thauer and colleagues (Thauer et al., 1977), but this was not confirmed here. Wenk et al. (2017) focus on rubrerythrin (+23 mV), though to date this protein is known only to play a role in oxygen detoxification (Coulter et al., 1999; Kurtz, 2006). We do observe small shifts in the abundance of the menaquinones themselves, and in the cellular NAD(P)(H) pools (Figure S2A). Indeed, the proteomic approach here does not resolve such changes, which may occur at the scale of electron flux to/through key redox carriers (e.g., ferredoxin, menaquinones, and NAD(P)(H)). In such a scenario, the total number

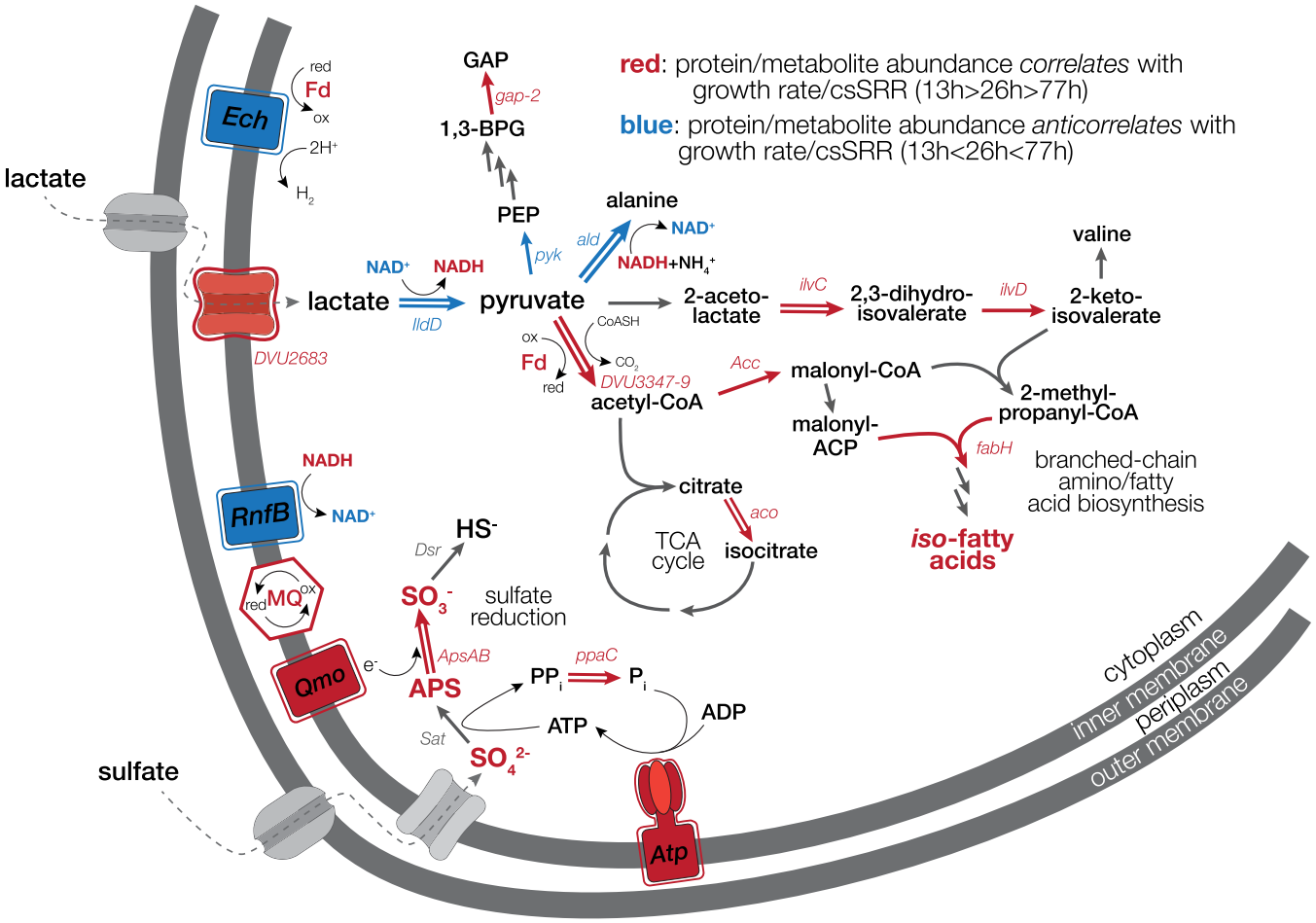

FIGURE 5 A schematic summary of observed protein and metabolite abundance changes in *Dv*H with rate modulation in lactate-limited chemostats. This summary focuses on sulfur, carbon, and energy metabolism. The abundance of proteins/metabolites highlighted in red correlates with csSRR (and inversely correlated with $^{34}\varepsilon_{SO4/H2S}$); the abundance of blue anti correlated with csSRR (and correlated with $^{34}\varepsilon_{SO4/H2S}$). For proteins, a double arrow or outline indicates that the abundance difference between the 13- and 77-h rates is significant at $q < 0.05$.

of and average redox state of electron transfer intermediates sets the capacity for energy transduction, which the cell increases or decreases as necessitated by environmental conditions.

Though shifts in proteomic and metabolite profiles indicate changes in the flow of energy through the electron transport chain, the extent to which shifts in electron carriers occur (Bertran et al., 2020; Sim et al., 2019; Wenk et al., 2017), particularly at extremely low energy fluxes, remains experimentally under-constrained. Follow-up studies should work to directly quantify the total abundance and the oxidized/reduced ratios of the key players under a range of energy (and ultimately power) limitations, and such work must also incorporate the most complete understanding of core SRB biochemistry (e.g., Barbosa et al., 2024; Bradley et al., 2011; Santos et al., 2015). To further explore the relationship between net S-isotope fractionation, intracellular isotopic compositions, proteins, and metabolic flux balance, we suggest the chemostat and associated analytical approaches employed herein be repeated at even more extreme energy (or sulfate, or nutrient) limitations as have been tested previously (Leavitt et al., 2013; Sim et al., 2011).

5 | CONCLUSIONS

The coordinated shifts in proteins and metabolites underpin the nonlinear relationship between the observed csSRR and $^{34}\varepsilon_{SO4/H2S}$ (c.f. Figure 1, Figure S4). We show that DvH modulates the composition of its membrane, electron carriers, and redox active proteins in response to the different energy flux regimes imposed upon it (Figures 2–4, Figure S2). Collectively, this modulates the expressed S and H isotope fractionation values for catabolism and anabolism, respectively, each as they relate to central energy metabolism and csSRR, presenting unique "isotopic phenotypes" (Pellerin et al., 2015, 2018). The availability of energy in any environment dictates the ecological and geochemical responses of the local microbial community. In chemostat experiments with the well-studied sulfate reducer *Desulfovibrio vulgaris* Hildenborough, the lipid, protein, and redox active metabolites respond coherently to differences in power availability, which yield distinct and predictable shifts in cell-specific respiration rate, lipid/water H, and sulfate/sulfide S isotope values. While it remains to be

understood how precisely the biochemical reactions sum up and translate into the inverse relationship between respiration rate and specifically S-isotope fractionation, the cells respond in real time to the influx of energy and can modulate a wide range of their electron transport chain and shift the standing stocks of respiration intermediates.

This work informs our understanding of how sulfate reducers tune their metabolism to the flow of available energy, and the downstream consequences for stable isotope ratios in organic and inorganic molecules. To incorporate these findings into metabolic isotope model, the quantities of both MSR reaction intermediates and electron transfer proteins must be carefully calibrated in response to a much wider range of power availabilities reflecting those in natural systems, where life operates close to the thermodynamic limit (Hoehler et al., 2023; Hoehler & Jørgensen, 2013), tuned to incorporate natural abundance stable isotopic constraints, as well as a more diverse array of sulfate reducers or metabolisms operating near the thermodynamic limit. The combination of experimental and analytical approaches employed here offers a fresh look at the cellular mechanisms that underpin Earth's S and C cycles through the lens of dissimilatory sulfate reduction. The merger of careful physiological work with isotopic analyses will enable us to calibrate metabolic isotope models, both in the MSR system, as well as microbial metabolisms that regulate elemental cycles at a planetary scale.

ACKNOWLEDGMENTS

We thank S. Moore and D. Fike for bulk sulfur isotope analyses (WashU); M. Seuss for assistance with lipid-H isotope analyses (Bradley lab, WashU); X. Feng (Dartmouth) and M. Osburn (Northwestern) for water H-isotope analyses; and A. Sessions and J. Adkins (CalTech) for access to HPLC-ICP-MS. Metabolite analyses were performed by the Proteomics & Mass Spectrometry Facility at the Danforth Plant Science Center (St. Louis, MO, USA). Funding was provided: by NASA Exobiology Award 13-EXO13-0082 (ASB, WDL, JW), NSF-EAR Award 1928309 (WDL), Washington University in St. Louis Department of Earth & Planetary Sciences Fossett Fellowship (WDL), the Walter and Constance Burke Fund at Dartmouth College (WDL), and the Fulbright—Bunge & Born—Williams Foundation Scholarship Program (FJB), Fundação para a Ciência e Tecnologia (Portugal) through R&D unit MOSTMICRO-ITQB (UIDB/04612/2020 and UIDP/04612/2020) and LS4FUTURE Associated Laboratory (LA/P/0087/2020) (IACP), NSF GRFP [2017250547] (SP).

CONFLICT OF INTEREST STATEMENT

The authors declare no conflicts of interest.

DATA AVAILABILITY STATEMENT

Proteomic data: Proteomic mass spectral data are available via proteomeXchange under accession PXD027511 and the MassIVE repository (massive.ucsd.edu) under accession MSV000087869. Other Data: https://doi.org/10.6084/m9.figshare.23989398.v1 for data and supplemental information.

ORCID

William D. Leavitt https://orcid.org/0000-0002-7909-2475
Jacob Waldbauer https://orcid.org/0000-0002-0338-6143
Sofia S. Venceslau https://orcid.org/0000-0001-8774-1351
Min Sub Sim https://orcid.org/0000-0002-3491-9002
Flavia Jaquelina Boidi https://orcid.org/0000-0001-7135-8745

REFERENCES

Arrivault, S., Guenther, M., Ivakov, A., Feil, R., Vosloh, D., van Dongen, J. T., Sulpice, R., & Stitt, M. (2009). Use of reverse-phase liquid chromatography, linked to tandem mass spectrometry, to profile the Calvin cycle and other metabolic intermediates in *Arabidopsis rosettes* at different carbon dioxide concentrations. *The Plant Journal*, *59*, 826–839.

Badzjong, W., & Thauer, R. K. (1980). Vectorial electron transport in *Degulfovibrio vulgaris* (Marburg) growing on hydrogen plus sulfate as sole energy source. *Archives of Microbiology*, *125*, 167–174.

Barbosa, A. C. C., Venceslau, S. S., & Pereira, I. A. C. (2024). DsrMKJOP is the terminal reductase complex in anaerobic sulfate respiration. *Proceedings of the National Academy of Sciences of the United States of America*, *121*, e2313650121.

Benjamini, Y., & Hochberg, Y. (1995). Controlling the false discovery rate: A practical and powerful approach to multiple testing. *Journal of the Royal Statistical Society: Series B: Methodological*, *57*, 289–300.

Berner, R. A., & Canfield, D. E. (1989). A new model for atmospheric oxygen over phanerozoic time. *American Journal of Science*, *289*, 333–361.

Bertran, E., Waldeck, A., Wing, B., Halevy, I., Leavitt, W., Bradley, A., & Johnston, D. (2020). Oxygen isotope effects during microbial sulfate reduction: Applications to sediment cell abundances. *The ISME Journal*, *14*, 1–12.

Bosdriesz, E., Molenaar, D., Teusink, B., & Bruggeman, F. J. (2015). How fast-growing bacteria robustly tune their ribosome concentration to approximate growth-rate maximization. *The FEBS Journal*, *282*, 2029–2044.

Bowles, M. W., Mogollón, J. M., Kasten, S., Zabel, M., & Hinrichs, K.-U. (2014). Global rates of marine sulfate reduction and implications for sub–sea-floor metabolic activities. *Science*, *344*, 889–891.

Bradley, A., Leavitt, W., & Johnston, D. (2011). Revisiting the dissimilatory sulfate reduction pathway. *Geobiology*, *9*, 446–457.

Bradley, A., Leavitt, W., Schmidt, M., Knoll, A. H., Girguis, P. R., & Johnston, D. T. (2016). Patterns of sulfur isotope fractionation during microbial sulfate reduction. *Geobiology*, *14*, 91–101.

Bradley, J., Arndt, S., Amend, J., Burwicz, E., Dale, A. W., Egger, M., & LaRowe, D. (2020). Widespread energy limitation to life in global subseafloor sediments. *Science Advances*, *6*, eaba0697.

Brunner, B., & Bernasconi, S. M. (2005). A revised isotope fractionation model for dissimilatory sulfate reduction in sulfate reducing bacteria. *Geochimica et Cosmochimica Acta*, *69*, 4759–4771.

Campbell, B. J., Li, C., Sessions, A. L., & Valentine, D. L. (2009). Hydrogen isotopic fractionation in lipid biosynthesis by H2-consuming *Desulfobacterium autotrophicum*. *Geochimica et Cosmochimica Acta*, *73*, 2744–2757.

Campbell, B. J., Sessions, A. L., Fox, D. N., Paul, B. G., Qin, Q., Kellermann, M. Y., & Valentine, D. L. (2017). Minimal influence of [NiFe] hydrogenase on hydrogen isotope fractionation in H2-oxidizing cupriavidus necator. *Frontiers in Microbiology*, *8*, 1886.

Chambers, L. A., Trudinger, P. A., Smith, J. W., & Burns, M. S. (1975). Fractionation of sulfur isotopes by continuous cultures of *Desulfovibrio desulfuricans*. *Canadian Journal of Microbiology*, *21*, 1602–1607.

Christensen, G., Zane, G., Kazakov, A., Li, X., Rodionov, D., Novichkov, P., Dubchak, I., Arkin, A. P., & Wall, J. D. (2015). Rex (encoded by

DVU_0916) in *Desulfovibrio vulgaris* Hildenborough is a repressor of sulfate adenylyl transferase and is regulated by NADH. *Journal of Bacteriology*, *197*, 29–39.

Cline, J. D. (1969). Spectrophotometric determination of hydrogen sulfide in natural waters. *Limnology and Oceanography*, *14*, 454–458.

Coulter, E., Shenvi, N., & Kurtz, D., Jr. (1999). NADH peroxidase activity of rubrerythrin. *Biochemical and Biophysical Research Communications*, *255*, 317–323.

Dawson, K. S., Osburn, M. R., Sessions, A. L., & Orphan, V. J. (2015). Metabolic associations with archaea drive shifts in hydrogen isotope fractionation in sulfate-reducing bacterial lipids in cocultures and methane seeps. *Geobiology*, *13*, 462–477.

Drake, H., Whitehouse, M. J., Heim, C., Reiners, P. W., Tillberg, M., Hogmalm, K. J., Dopson, M., Broman, C., & Åström, M. E. (2018). Unprecedented 34S-enrichment of pyrite formed following microbial sulfate reduction in fractured crystalline rocks. *Geobiology*, *16*, 556–574.

Farquhar, J., Johnston, D. T., & Wing, B. A. (2007). Implications of conservation of mass effects on mass-dependent isotope fractionations: Influence of network structure on sulfur isotope phase space of dissimilatory sulfate reduction. *Geochimica et Cosmochimica Acta*, *71*, 5862–5875.

Fike, D. A., Bradley, A. S., & Rose, C. V. (2015). Rethinking the ancient sulfur cycle. *Annual Review of Earth and Planetary Sciences*, *43*, 593–622.

García, A., Ferrer, P., Albiol, J., Castillo, T., Segura, D., & Peña, C. (2018). Metabolic flux analysis and the NAD (P) H/NAD (P)+ ratios in chemostat cultures of *Azotobacter vinelandii*. *Microbial Cell Factories*, *17*, 1–13.

Goldhaber, M., & Kaplan, I. (1975). Controls and consequences of sulfate reduction rates in recent marine sediments. *Soil Science*, *119*, 42–55.

Hayes, J. M., & Waldbauer, J. R. (2006). The carbon cycle and associated redox processes through time. *Philosophical Transactions of the Royal Society of London. Series B, Biological Sciences*, *361*, 931–950.

Hoehler, T. M., & Jørgensen, B. B. (2013). Microbial life under extreme energy limitation. *Nature Reviews Microbiology*, *11*, 83–94.

Hoehler, T. M., Mankel, D. J., Girguis, P. R., McCollom, T. M., Kiang, N. Y., & Jørgensen, B. B. (2023). The metabolic rate of the biosphere and its components. *Proceedings of the National Academy of Sciences of the United States of America*, *120*, e2303764120.

Jaussi, M., Jørgensen, B. B., Kjeldsen, K. U., Lomstein, B. A., Pearce, C., Seidenkantz, M.-S., & Røy, H. (2023). Cell-specific rates of sulfate reduction and fermentation in the sub-seafloor biosphere. *Frontiers in Microbiology*, *14*. https://doi.org/10.3389/fmicb.2023.1198664

Johnston, D. T., Farquhar, J., & Canfield, D. E. (2007). Sulfur isotope insights into microbial sulfate reduction: When microbes meet models. *Geochimica et Cosmochimica Acta*, *71*, 3929–3947.

Jørgensen, B. B. (1982). Mineralization of organic matter in the sea bed—The role of sulphate reduction. *Nature*, *296*, 643–645.

Jørgensen, B. B., Findlay, A. J., & Pellerin, A. (2019). The biogeochemical sulfur cycle of marine sediments. *Frontiers in Microbiology*, *10*. https://doi.org/10.3389/fmicb.2019.00849

Jørgensen, B. B., & Marshall, I. P. G. (2016). Slow microbial life in the seabed. *Annual Review of Marine Science*, *8*, 311–332.

Klumpp, S., Scott, M., Pedersen, S., & Hwa, T. (2013). Molecular crowding limits translation and cell growth. *Proceedings of the National Academy of Sciences of the United States of America*, *110*, 16754–16759.

Kurtz, D. M., Jr. (2006). Avoiding high-valent iron intermediates: Superoxide reductase and rubrerythrin. *Journal of Inorganic Biochemistry*, *100*, 679–693.

LaRowe, D. E., Arndt, S., Bradley, J. A., Burwicz, E., Dale, A. W., & Amend, J. P. (2020). Organic carbon and microbial activity in marine sediments on a global scale throughout the Quaternary. *Geochimica et Cosmochimica Acta*, *286*, 227–247.

Leavitt, W. D., Cummins, R., Schmidt, M. L., Sim, M. S., Ono, S., Bradley, A. S., & Johnston, D. T. (2014). Multiple sulfur isotope signatures of sulfite and thiosulfate reduction by the model dissimilatory sulfate-reducer, *Desulfovibrio alaskensis* str. G20. *Frontiers in Microbiology*, *5*, 591.

Leavitt, W. D., Flynn, T. M., Suess, M. K., & Bradley, A. S. (2016). Transhydrogenase and growth substrate influence lipid hydrogen isotope ratios in *Desulfovibrio alaskensis* G20. *Frontiers in Microbiology*, *7*, 918.

Leavitt, W. D., Halevy, I., Bradley, A. S., & Johnston, D. T. (2013). Influence of sulfate reduction rates on the phanerozoic sulfur isotope record. *Proceedings of the National Academy of Sciences of the United States of America*, *110*, 11244–11249.

Leavitt, W. D., Murphy, S. J.-L., Lynd, L. R., & Bradley, A. S. (2017). Hydrogen isotope composition of *Thermoanaerobacterium saccharolyticum* lipids: Comparing wild type with a *nfn*-transhydrogenase mutant. *Organic Geochemistry*, *113*, 239–241.

Leavitt, W. D., Venceslau, S. S., Pereira, I. A., Johnston, D. T., & Bradley, A. S. (2016). Fractionation of sulfur and hydrogen isotopes in *Desulfovibrio vulgaris* with perturbed DsrC expression. *FEMS Microbiology Letters*, *363*, fnw226.

Leavitt, W. D., Venceslau, S. S., Waldbauer, J., Smith, D. A., Pereira, I. A. C., & Bradley, A. S. (2019). Proteomic and isotopic response of *Desulfovibrio vulgaris* to DsrC perturbation. *Frontiers in Microbiology*, *10*, 658.

Lever, M. A., Rogers, K. L., Lloyd, K. G., Overmann, J., Schink, B., Thauer, R. K., Hoehler, T. M., & Jørgensen, B. B. (2015). Life under extreme energy limitation: A synthesis of laboratory-and field-based investigations. *FEMS Microbiology Reviews*, *39*, 688–728.

Lloyd, M., McClelland, H., Antler, G., Bradley, A., Halevy, I., Junium, C., Wankel, S. D., & Zerkle, A. L. (2020). The isotopic imprint of life on an evolving planet. *Space Science Reviews*, *216*, 1–54.

Lunn, J. E., Feil, R., Hendriks, J. H., Gibon, Y., Morcuende, R., Osuna, D., Scheible, W. R., Carillo, P., Hajirezaei, M. R., & Stitt, M. (2006). Sugar-induced increases in trehalose 6-phosphate are correlated with redox activation of ADPglucose pyrophosphorylase and higher rates of starch synthesis in *Arabidopsis thaliana*. *Biochemical Journal*, *397*, 139–148.

McFarlin, J. M., Axford, Y., Masterson, A. L., & Osburn, M. R. (2019). Calibration of modern sedimentary δ2H plant wax-water relationships in Greenland lakes. *Quaternary Science Reviews*, *225*, 105978.

Osburn, M. R., Dawson, K. S., Fogel, M. L., & Sessions, A. L. (2016). Fractionation of hydrogen isotopes by sulfate-and nitrate-reducing bacteria. *Frontiers in Microbiology*, *7*, 1166.

Paris, G., Sessions, A. L., Subhas, A. V., & Adkins, J. F. (2013). MC-ICP-MS measurement of δ34S and Δ33S in small amounts of dissolved sulfate. *Chemical Geology*, *345*, 50–61.

Pellerin, A., Anderson-Trocmé, L., Whyte, L. G., Zane, G. M., Wall, J. D., & Wing, B. A. (2015). Sulfur isotope fractionation during the evolutionary adaptation of a sulfate-reducing bacterium. *Applied and Environmental Microbiology*, *81*, 2676–2689.

Pellerin, A., Wenk, C. B., Halevy, I., & Wing, B. A. (2018). Sulfur isotope fractionation by sulfate-reducing microbes can reflect past physiology. *Environmental Science & Technology*, *52*, 4013–4022.

Ramos, A. R., Grein, F., Oliveira, G. P., Venceslau, S. S., Keller, K. L., Wall, J. D., & Pereira, I. A. C. (2015). Role of FlxABCD-HdrABC in Desulfovibrio vulgaris. *Environ Microbiol*, *17*, 2288–2305. https://doi.org/10.1111/1462-2920.12689

Rees, C. (1973). A steady-state model for sulphur isotope fractionation in bacterial reduction processes. *Geochimica et Cosmochimica Acta*, *37*, 1141–1162.

Santos, A. A., Venceslau, S. S., Grein, F., Leavitt, W. D., Dahl, C., Johnston, D. T., & Pereira, I. A. (2015). A protein trisulfide couples dissimilatory sulfate reduction to energy conservation. *Science*, *350*, 1541–1545.

Sim, M. S., Bosak, T., & Ono, S. (2011). Large sulfur isotope fractionation does not require disproportionation. *Science*, *333*, 74–77.

Sim, M. S., Ogata, H., Lubitz, W., Adkins, J. F., Sessions, A. L., Orphan, V. J., & McGlynn, S. E. (2019). Role of APS reductase in biogeochemical sulfur isotope fractionation. *Nature Communications*, *10*, 44.

Sim, M. S., Paris, G., Adkins, J. F., Orphan, V. J., & Sessions, A. L. (2017). Quantification and isotopic analysis of intracellular sulfur metabolites in the dissimilatory sulfate reduction pathway. *Geochimica et Cosmochimica Acta*, *206*, 57–72.

Sim, M. S., Woo, D. K., Kim, B., Jeong, H., Joo, Y. J., Hong, Y. W., & Choi, J. Y. (2023). What controls the sulfur isotope fractionation during dissimilatory sulfate reduction? *ACS Environmental Au*, *3*, 76–86.

Taenzer, L., Labidi, J., Masterson, A. L., Feng, X., Rumble, D., III, Young, E. D., & Leavitt, W. D. (2020). Low Δ12CH2D2 values in microbialgenic methane result from combinatorial isotope effects. *Geochimica et Cosmochimica Acta*, *285*, 225–236.

Thauer, R. K., Jungermann, K., & Decker, K. (1977). Energy conservation in chemotrophic anaerobic bacteria. *Bacteriological Reviews*, *41*, 100–180.

Thode, H. G., Monster, J., & Dunford, H. B. (1961). Sulphur isotope geochemistry. *Geochimica et Cosmochimica Acta*, *25*, 159–174.

Waldbauer, J., Zhang, L., Rizzo, A., & Muratore, D. (2017). diDO-IPTL: A peptide-labeling strategy for precision quantitative proteomics. *Analytical Chemistry*, *89*, 11498–11504.

Wenk, C. B., Wing, B. A., & Halevy, I. (2017). Electron carriers in microbial sulfate reduction inferred from experimental and environmental sulfur isotope fractionations. *The ISME Journal*, *12*, 495–507.

Wijker, R. S., Sessions, A. L., Fuhrer, T., & Phan, M. (2019). 2H/1H variation in microbial lipids is controlled by NADPH metabolism. *Proceedings of the National Academy of Sciences of the United States of America*, *116*, 12173–12182.

Wing, B. A., & Halevy, I. (2014). Intracellular metabolite levels shape sulfur isotope fractionation during microbial sulfate respiration. *Proceedings of the National Academy of Sciences of the United States of America*, *111*, 18116–18125.

SUPPORTING INFORMATION

Additional supporting information can be found online in the Supporting Information section at the end of this article.

How to cite this article: Leavitt, W. D., Waldbauer, J., Venceslau, S. S., Sim, M. S., Zhang, L., Boidi, F. J., Plummer, S., Diaz, J. M., Pereira, I. A. C., & Bradley, A. S. (2024). Energy flux couples sulfur isotope fractionation to proteomic and metabolite profiles in *Desulfovibrio vulgaris*. *Geobiology*, *22*, e12600. https://doi.org/10.1111/gbi.12600